Surface Charge and Coating of $CoFe_2O_4$ Nanoparticles: Evidence of Preserved Magnetic and Electronic Properties

Silvia Nappini,[a] Elena Magnano,[a] Federica Bondino,[a] Igor Píš,[a,b] Alessandro Barla,[c] Elvira Fantechi,[d] Francesco Pineider,[d] Claudio Sangregorio,[e] Lisa Vaccari,[b] Leonardo Venturelli,[a] and Piero Baglioni[f].*

[a]Laboratorio TASC, IOM CNR, S.S. 14 km 163.5, 34149 Basovizza, Trieste, Italy

[b] Elettra Synchrotron Trieste, S.S. 14 km 163.5, 34149 Basovizza, Trieste, Italy

[c]Istituto di Struttura della Materia, ISM CNR, S.S. 14 km 163.5, 34149 Basovizza, Trieste, Italy

[d]INSTM and Department of Chemistry, via della Lastruccia 3, 50019 Sesto F.no, Florence, Italy

[e]INSTM and ICCOM CNR, Via Madonna del Piano 10, 50019 Sesto F.no, Florence, Italy

[f]CSGI and Department of Chemistry, via della Lastruccia 3, 50019 Sesto F.no, Florence, Italy

KEYWORDS magnetic nanoparticles, hyperthermia, X-ray absorption spectroscopy (XAS), X-ray magnetic circular dichroism (XMCD), X-ray photoemission spectroscopy (XPS).

ABSTRACT

Magnetic nanoparticles (MNPs) have shown exceptional potential for several biological and clinical applications. However, MNPs must be coated by a biocompatible shell for such applications. The aim of this study is to understand if and how the surface charge and coating can affect the electronic and magnetic properties of $CoFe_2O_4$ MNPs. A detailed spectroscopic study of the electronic, and magnetic properties of three differently functionalized $CoFe_2O_4$ NPs is reported. Positively and negatively charged uncoated $CoFe_2O_4$ NPs, as well as citrate-coated NPs were prepared by soft chemistry synthesis. The size and the shape of the NPs were investigated by means of Small Angle X-ray Scattering (SAXS) and Transmission Electron Microscopy (TEM) measurements, and the electronic properties and cationic distribution of $CoFe_2O_4$ NPs were probed by X-ray Absorption (XAS), X-ray Magnetic Circular Dichroism (XMCD) and X-ray Photoemission Spectroscopy (XPS) techniques. The surface functionalization with citric acid was confirmed by infrared spectroscopy, and the overall magnetic behavior was evaluated by magnetometry. The hyperthermic properties of the differently functionalized $CoFe_2O_4$ NPs was evaluated through calorimetric measurements in the presence of an alternating magnetic field. The results showed a high effective magnetic anisotropy energy in all the investigated magnetic NPs, highlighting their potential use for hyperthermia. In addition, the different investigation techniques have shown that the citrate coating improves the stability of the NPs in aqueous environment, making $CoFe_2O_4$ NPs suitable for biomedical applications, without affecting their electronic and magnetic properties.

1. Introduction

Magnetic nanoparticles (MNPs) have risen great interest because of their remarkable magnetic, electric, physical and chemical properties, which, in most cases, are different from those of the bulk materials. Thanks to their intriguing properties, MNPs have found applicability in many different areas, such as fabrication of electronic components for information storage, magnetic cards, recording devices, catalysis[1–5], and, when properly functionalized, they represent a promising approach for drug delivery, magnetic fluid hyperthermia (MFH), magnetic resonance imaging (MRI), tissue engineering and bioanalysis[6–12]. In particular, magnetic spinel ferrites ($M_xFe_{3-x}O_4$, where M = Fe, Co, Ni, Mn or Zn) are emerging as innovative nanostructures for many biological applications, where a superparamagnetic behaviour, a high magnetization value, a diameter smaller than a critical value (typically around 10-20 nm), a narrow size distribution and an appropriate surface coating are required. Among magnetic spinel ferrite NPs, $CoFe_2O_4$ has received a lot of attention for its unique magnetic properties, such as a large anisotropy energy, tuneable coercivity and high saturation magnetization, that make $CoFe_2O_4$ NPs good candidates to be used for MRI and MFH[10,11].

For applications, such as MRI, MFH and drug delivery, the ability to control magnetic anisotropy, together with the possibility of controlling NP size and surface composition could provide a method to optimize the NP relaxation time for a specific applied field frequency. Large heating effects are essential to realize magnetic-based therapeutic treatments; however, a biocompatible coating to prevent NP aggregation without affecting the magnetic properties is essential for biomedical applications of $CoFe_2O_4$ NPs.

Bulk ferrites normally adopt the typical cubic spinel arrangement, where the trivalent and divalent ions occupy 16 of the 64 octahedral sites (O_h) and 8 of the 32 tetrahedral sites (T_d).

Depending on the cation distributions, ferrites are classified as normal or inverse spinels: in the first ones, the trivalent ions sit on O_h cavities, while divalent ions occupy T_d sites; in the second ones, trivalent ions are distributed between T_d and O_h cavities, while the 8 divalent ions occupy the remaining O_h sites. However, it has been found that most of mixed ferrites, such as $CoFe_2O_4$, exhibit only partially inverted spinel structure. At the nanoscale level, the inversion degree, corresponding to the fraction of divalent ions in O_h sites, can significantly depend on synthesis conditions, especially on the Co/Fe ratio in the precursor solution and the reaction temperature[13–15]. The replacement of Fe^{2+} cations with the more anisotropic Co^{2+} cations allows an increase in the magneto-crystalline anisotropy up to 20 times in comparison with that of magnetite.

The magnetic properties of ferrites depend on many factors, including the composition, the cation distribution into the crystallographic structure, the shape, the size, and the surface morphology[16,17].

The shape of the NPs is an additional parameter that can bring a contribution to the total magnetic anisotropy of the material. In the absence of an applied magnetic field, a magnetically isotropic material has no preferential direction for its magnetic moment, while a magnetically anisotropic material will align its moment with one of the easy axes. In fact, when a particle is not perfectly spherical, the demagnetizing field will not be equal for all directions.

Also the size of the NPs has an important effect on the magnetic properties. For decreasing diameters, the surface area becomes larger with respect to the bulk, and thus more cations are located near the surface, resulting in a greater disordered distribution of the electron spins on the surface because of their reduced spin-spin exchange[17,18].

The alteration of the surface morphology is another parameter that might change the cation distributions among T_d and O_h sites and consequently the magnetic properties of NPs.

The surface morphology could be modified by the presence of a coating shell, which is fundamental for biomedical applications. The surface coating can regulate the physical and chemical stability of the system, preventing NP aggregation in physiological environment, and providing also a higher biocompatibility.

The NP coating is generally obtained by chemical functionalization with organic or inorganic ligands, polymers, surfactants, dextran and phospholipids[19–23]. The nature of the surface shell can affect the water accessibility to the magnetic core, influencing also the magnetic properties and relaxivity of the MNPs.

Despite several studies on the structural characterization of $CoFe_2O_4$ NPs have already been done, little is reported on their electronic and magnetic properties as a function of different surface functionalization. However, a deeper understanding of the electronic, geometric, magnetic, chemical and physical properties of $CoFe_2O_4$ NPs is fundamental for their applicability in different fields of research.

In this paper, we report a detailed investigation on the structure, oxidation state, electronic and magnetic properties of $CoFe_2O_4$ NPs with three different types of stabilization: positively and negatively charged uncoated NPs, and citrate coated NPs. These types of NPs are stable and well dispersed in aqueous solution because of the electrostatic repulsion achieved by surrounding NPs with ionic species and surface functionalization with a capping agent (citric acid). Citrate coating is widely used to obtain stable NPs in physiological solution thanks to the presence of terminal water-exposed carboxylate groups, which also provide good anchoring sites for further surface functionalization (i.e. with fluorescent dyes or molecules of biomedical interest).

All the investigated samples were obtained by soft chemistry synthesis, as reported in detail in the experimental section. The size, shape and morphology of the NPs were investigated by

means of small angle X-ray scattering (SAXS) and transmission electron microscopy (TEM) measurements and the composition and the citrate coordination were determined by Inductively Coupled Plasma–Atomic Emission (ICP-AES) and Attenuated Total Reflectance Fourier-Transform Infrared (ATR-FTIR) spectroscopy.

Information on the chemical states of Co and Fe cations of the $CoFe_2O_4$ NP samples, the effect of different surface charges, as well as the chemical bonding of the citrate shell were obtained by X-ray photoemission spectroscopy (XPS). A detailed analysis of the electronic properties, including the oxidation state, and distributions of Co and Fe cations over the T_d and Oh sites was performed by Soft X-ray Absorption Spectroscopy (XAS) and X-ray magnetic circular dichroism (XMCD) methods.

The overall magnetic behavior of both uncoated and citrate-coated $CoFe_2O_4$ NPs was evaluated by collecting hysteresis curves at 2.5 K with a vibrating sample magnetometer (VSM). In addition, the hyperthermic properties of the $CoFe_2O_4$ NPs samples, i.e. their capability to release heat when exposed to alternating magnetic field (AMF), was evaluated through calorimetric experiments.

2. Experimental Methods

Cobalt Ferrite Nanoparticle Synthesis. $CoFe_2O_4$ NPs were prepared according to the method developed by Massart[24], introducing minor modifications as previously reported[6,7,25]. Solutions of 1 M $FeCl_3$ (64 ml) and $Co(NO_3)_2$ (32 ml) were added to concentrated nitric acid (2 ml). The mixture was heated to boiling point and then mixed under vigorous agitation with a boiling solution of NaOH 1M (400 ml). The boiling temperature (100 °C) and the stirring were maintained for 90 minutes. The obtained NPs were separated by magnetic decantation, washed

with water and resuspended on 40 ML of HNO_3 2M. After a second magnetic decantation, the NPs were dispersed in a boiling solution of 0.5 M $FeCl_3$ (56 ml) and 0.5 M $Co(NO_3)_2$ (28 ml) and kept under vigorous agitation for 30 minutes. The precipitate was isolated, washed with water and dispersed in 0.25 M TMAH (tetramethylammonium hydroxide solution), obtaining negatively charged $CoFe_2O_4$ NPs. Positively charged $CoFe_2O_4$ NPs were obtained by washing the precipitate with HNO_3 1 M (30 ml) and dispersing it in water

Citrate-coated cobalt ferrite NPs were prepared starting from the uncoated NPs dispersed in TMAH by coordination of citric acid. Uncoated MNPs (10 ml, 1% wt) were added to a 100 mM citric acid solution (30 ml) and slightly stirred for 1 h at room temperature (the resulting pH was around 5). After recollecting the precipitate with the magnet, NPs were dispersed in 20 mM tri-sodium citrate (30 ml) and kept under stirring for 45 min. The obtained particles were separated by magnetic decantation and washed several times with water and acetone in order to remove any excess of citric acid. The citrate coated MNPs were gently dried under a nitrogen gas flux, dispersed in the buffer solution (10 mM HEPES, 107 mM NaCl, 5.3 mM NaOH, pH 7.4) and kept under slight stirring for 24 h. The dispersion was finally centrifuged at 1000 g for 2 min and the supernatant was dialyzed against water for 24 h through a cellulose dialysis bag (avg. flat width 23 mm, MWCO 12400, 99.99% retention) in order to remove non-coordinated citrate species. A residual ionic strength is, however, always present because of solvated anions in equilibrium with the adsorbed ones. The citrate coordination of the metals on $CoFe_2O_4$ NP surface was verified by ATR-FTIR spectroscopy.

X-ray Absorption (XAS), X-ray Magnetic Circular Dichroism (XMCD) and X-ray Photoemission Spectroscopy (XPS). XAS, XMCD and XPS measurements were carried out at the BACH beamline (Beamline for Advanced diCHroism) at Elettra synchrotron facility in

Trieste (Italy). Due to the limitation of XAS, XMCD and XPS to UHV conditions, samples were dried prior to the measurements. Specifically, samples were prepared by dropcast method, where a drop of $CoFe_2O_4$ NPs suspension was deposited onto a clean Si wafer and left to dry. The experimental data were collected under UHV conditions (base pressure $\geq 1 \times 10^{-10}$ mbar) and with a photon flux of 10^{12} photons/s.

XAS spectra at the $L_{3,2}$ edges of Fe and Co, and K edge of O were measured both in total electron yield (TEY) mode and in total fluorescence yield (TFY) mode, ensuring both surface and bulk sensitivities, respectively. TEY spectra were recorded by measuring the drain current with an energy resolution better than 0.1 eV, TFY spectra were recorded using a silicon photodiode with an energy resolution better than 0.16 eV.

XMCD measurements in a high magnetic fields (up to 3 T) along the beam direction at a temperature of 11 K and 150 K, were carried out on negative uncoated $CoFe_2O_4$ NPs. The polarization of the incident light was flipped between the positive (σ+) and negative (σ-) photon helicity and the spectra were recorded in TEY mode.

XPS angle integrated spectra of Fe 2p and Co 2p, as well as O 1s core levels were collected at RT using a hemispherical electron energy analyzer Scienta R3000, with a total energy resolution of 130 meV, in normal emission geometry , with an angle of 60° between the incident light and the normal to the surface. Co 2p and Fe 2p spectra were measured at a photon energy of 1099 eV, while O 1s spectrum was measured at a photon energy of 734 eV. The O 1s spectra were fitted using Voigt functions and Shirley type background[26].

The XAS and XMCD signals were simulated by Ligand Field Multiplet (LFM) calculation and compared to the experimental XAS spectra in order to elucidate the origin of the different spectral features. The LFM model calculates the spectra of each cation in a given crystal field

(octahedral or tetrahedral symmetry), giving the oxidation state and quantitative information about the site occupancy of each ion state. LFM simulations were carried out using the CTM4XAS 5.5 program including full spin-orbit coupling, crystal field effects, and the reduction of the Slater integrals *F(dd)*, *F(pd)* and *G(pd)* to consider the electronic repulsions[27].

Inductively Coupled Plasma–Atomic Emission Spectrometry (ICP-AES). A VARIAN 720 OES inductively coupled plasma optical emission spectrometer (ICP-AES) was used for the determination of iron and cobalt content (ppm) of $CoFe_2O_4$ NP dispersions. The samples were diluted from 0.1 ml to 5.0 ml in 0.1% nitric acid. Calibration curves of standard solutions of iron and cobalt were used. The ICP-AES was programmed to detect Co (238.892; 228.615; 230.786 nm) and Fe (238.204; 259.940; 234.350 nm) and to give the average value of the obtained results for each metal. An internal standard of Ge 5 ppm (209.426 nm) was used to correct for matrix effects.

Transmission Electron Microscopy (TEM). TEM investigations were carried out using a Philips CM 12 electron microscope operating at acceleration voltages up to 120 kV and equipped with an Olympus MegaViewG2 side-mounted CCD camera. Samples were prepared by placing drops of the suspensions on a carbon-coated copper grid with a carbon membrane film and removing the excess solvent with filter paper.

Attenuated Total Reflection Infrared Spectroscopy (ATR-FTIR). FTIR spectra were collected using a VERTEX 70 interferometer (Bruker) purged with nitrogen and DTGS (deuterated tri glycine sulfate) detector. MIRacle Single Reflection ATR box (PIKE Technologies) equipped with a diamond IRE (Internal Reflection Element) was chosen for the purpose of the experiment. Five microliters of citrate coated CoF_2O_4 NPs dispersed in water were dropped onto the crystal and the measurements were repeated until vanishing of the

combination band of bending and vibrational modes of liquid water, centered at ~ 2150 cm^{-1}. The background was collected on the clean IRE element. Spectra were acquired averaging 128 scans with a spectral resolution of 4 cm^{-1}.

Small Angle X-Rays Scattering (SAXS). SAXS measurements were carried out with a HECUS SWAX-camera (Kratky) equipped with a position-sensitive detector (OED 50 M) containing 1024 channels of the width of 54 μm. Cu K_α radiation of wavelength 1.542 Å was obtained using an X-ray generator (Seifert ID-3003) operating at a maximum power of 2 kW. A 10 μm thick nickel filter was used to remove Cu K_α radiation. The volume between the sample and the detector was kept under vacuum (pressure less than 1 mBar) during measurements to minimize scattering from air. The liquid samples were filled into 1 mm quartz capillary and then sealed. Measurements were done at 25 °C and the temperature was controlled by a Peltier element, with an accuracy of ± 0.1 °C. All scattering curves were corrected for the solvent contribution. The data were slit desmeared by a linear method[28].

Magnetometry. Magnetic measurements were performed with a PPMS VSM magnetometer (Quantum Design, San Diego, USA) mounting a liquid helium cryostat and a superconducting coil magnet. The magnetization curves were recorded at 2.5 K and the data were corrected for the diamagnetic contribution of the sample holder which was measured separately.

Hyperthermic characterization. The hyperthermic properties of the $CoFe_2O_4$ NPs samples, were investigated by recording temperature kinetics during the exposition to an AMF. The experimental set-up was composed by a 6 kW Fives Celes® power supply, a water-cooled induction coil and a series of capacitors. The field parameters (183 kHz, 17.0 kA/m) were chosen in order to operate within the physiological limit, H ν<5 $10^9 Am^{-1}$ s^{-1}, beyond which deleterious responses of living tissues were observed[29]. Samples were placed in the middle of the induction

coil, hosted in a polystyrene sample holder inside a glass container thermostatized by a flow of ethylene glycol. The temperature of the samples, recorded by an optical fiber thermometer dipped into the sample, was allowed to stabilize to 25ºC prior to the measurement. The concentration of $CoFe_2O_4$ in the measured samples was 0.56% w/w for negative, 0.64% w/w for positive and 0.51% w/w for citrate. The Specific Absorption Rate(SAR) value, i.e. the power dissipated by the material as a function of the unit mass, was evaluated using the formula

$$SAR = \frac{c_{H_2O} m_{H_2O}}{m_{Me}} \frac{\Delta T}{\Delta t}$$

Where m_{Me} is the total mass of metals (Fe and Co), c_{H2O} and m_{H2O} the specific heat and mass of water, respectively. ΔT is the temperature increase in the interval of time Δt. Since the measurements are carried in non-adiabatic conditions, the $\Delta T/\Delta t$ value was extrapolated by taking the initial slope of the temperature kinetic curve.

3. Results and discussion

Structural and electronic characterization. Three types of $CoFe_2O_4$ NP samples (negatively, positively charged uncoated, and citrate coated MNPs) were prepared according to the Massart method (see Experimental Methods) and then functionalized with citric acid to obtain the citrate coated ones. All the samples are well dispersible in aqueous solution: the citrate coated NPs are particularly stable under physiological conditions thanks to the shell of citrate anions, while the alkaline ones are chemically stabilized by TMAH, that acts as a surfactant and peptizing agent creating an electrostatic repulsion layer surrounding the particles. Similarly, in the case of acidic

NPs, the electrostatic repulsion is achieved by protonation of the NP surface, through addition of HNO_3 to the alkaline dispersion.

A schematic picture of the stabilization of the investigated MNPs is depicted in Figure 1.

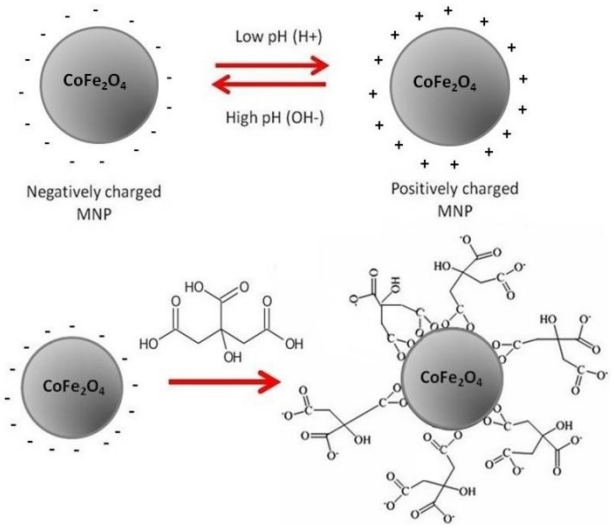

Figure 1. Scheme of the mechanism of stabilization of negatively, positively and citrate coated $CoFe_2O_4$ NPs.

The size, shape and morphology of uncoated and citrate-coated cobalt $CoFe_2O_4$ NPs were described and characterized in detail by means of TEM and SAXS.

TEM pictures and the corresponding size distributions are reported in Figure 2. They show that all the three NP samples are quite mono-disperse and their shape is nearly spherical. A comparison of the histograms shows that the diameter of the NPs is 7 ± 3 nm. It is important to point out that the citrate coating cannot be detected by TEM because of its low electronic density. TEM is restricted to small volumes and hence to low precipitate populations, making it poorly suited for statistical analysis[30].

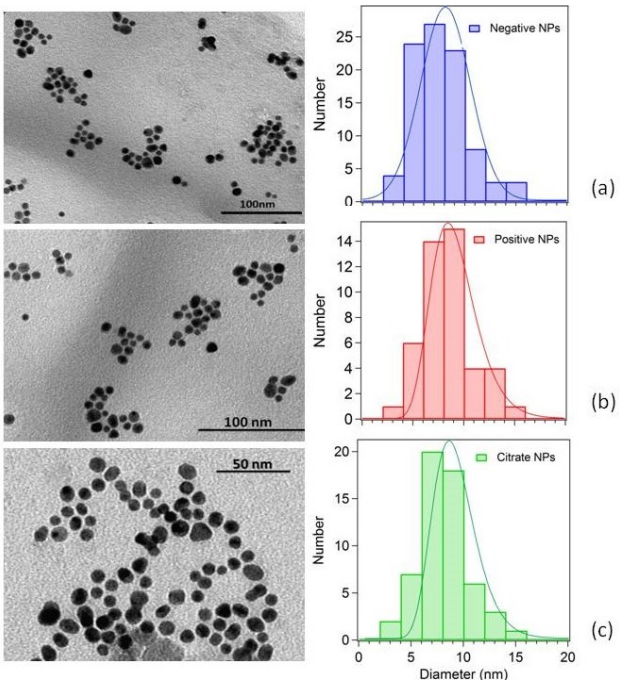

Figure 2. TEM images and the corresponding size distribution of (a) negatively charged uncoated, (b) positively charged uncoated and (c) citrate coated $CoFe_2O_4$ NPs .

In order to have information about the average diameter and the size distribution in aqueous solution, SAXS measurements were performed directly on the NPs dispersed in water. In comparison to TEM, SAXS benefits from higher statistical quality in the size distribution determination within one measurement and presents no limitation imposed by drying the sample, which can lead to aggregation or other physical change[30].

SAXS analysis of uncoated and citrate coated $CoFe_2O_4$ NPs were well described in previous works[6,7]. Briefly, SAXS spectra were modelled according to the formalism introduced by Bartlett and Ottewill for polydisperse spherical particles[31], where the particles are described as spherical objects with a Schulz distribution of radii[32,33]. No structure factors were included in this model because of the low concentration of particles in the dispersions, so that inter-particle interference effects can be neglected. The fitting results summarized in Table 1 shows that the obtained radii

of uncoated and citrate-coated NPs are very similar. This is due to the fact that the electronic density in $CoFe_2O_4$ NPs largely overrules that of the citrate shell, so SAXS signal accounts only for the metal oxide cores.

Table 1. Structural parameters of $CoFe_2O_4$ NPs dispersed in water obtained by SAXS. <D> stands for mean diameter.

	Citrate coated $CoFe_2O_4$	**Uncoated $CoFe_2O_4$(-)**	**Uncoated $CoFe_2O_4$(+)**
SAXS Fitting			
$\langle D \rangle$ [nm]	9.8 ± 0.2	11.2 ± 0.4	11.8 ± 0.4
Polydispersity	0.60 ± 0.01	0.49 ± 0.02	0.42 ± 0.01

Iron and Cobalt content in the three $CoFe_2O_4$ NP samples was checked by ICP-AES confirming the 2:1 ratio between Fe and Co in the oxide structure of the NPs. The concentration of the "as prepared" samples (mother solutions) are reported in the S.I., and eventually decreased by dilution for the experiments.

The surface functionalization of $CoFe_2O_4$ NPs with citrate was proved by ATR-FTIR measurements by comparing the NP spectrum with citric acid (ligand precursor) and tri-sodium citrate (reference) spectra to understand the mechanism of citrate coordination to NPs.

A comparison among the ATR-FTIR [34] spectra of citrate coated $CoFe_2O_4$ NPs (70 mM), tri-sodium citrate (20 mM) and citric acid (20 mM) aqueous solutions is shown in Figure 3 and the results are summarized in Table 2.

The intense peak centred at 1709 cm^{-1} in the spectrum of pure citric acid can be assigned to the carbonyl stretching of the carboxylic group (COOH). This contribution is totally suppressed in the spectrum of the pure tri-sodium citrate, characterized by two strong bands centred at 1572

and 1390 cm^{-1}, respectively assignable to asymmetric and symmetric stretching of carbonyl group of free-carboxylate anion (COO^-), and by a broad band centred at 1255 cm^{-1}, related to the combination of stretches and bends of carboxylate group[35].

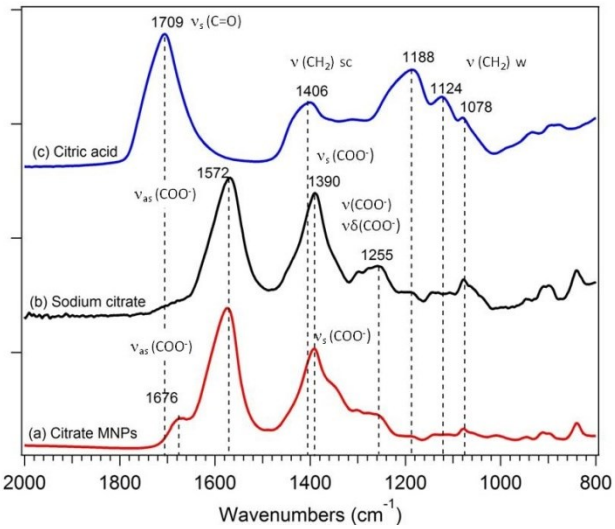

Figure 3. ATR-FTIR spectra of (a) citrate coated $CoFe_2O_4$ NPs at pH=7.4, (b) 20 mM trisodium citrate solution, and (c) 20 mM citric acid solution.

In addition to those peaks, the ATR-FTIR spectrum of citrate-coated NPs shows a band centred at 1676 cm^{-1}, that clearly indicates that citric acid binds to NP surface through coordination of the carboxylate functionalities of citrate anions, as already reported[36–39] . Indeed, carboxylic groups of citric acid chemisorbed onto the NP surface possess a partial single bond character that results in the weakening of the C=O bond and determines the shift to lower frequency of the stretching of the C=O group coordinated onto the surface of $CoFe_2O_4$. It is therefore possible to envision that citric acid forms complexes with the metal cations of $CoFe_2O_4$ by chemisorption of one or two of the three COO^- functionalities, depending on steric and curvature of the surface, while the residual carboxylate groups do not interact with NP[37,39], and therefore preserve characteristics of free carboxylate moieties. This coordination scheme is

further supported by the more pronounced asymmetry of the symmetric stretching of COO^- moieties, that indicates the presence of at least two types of $\sim\nu_{sym}(COO^-)$.

Table 2. FTIR vibrational assignments at citric acid, tri-sodium citrate and citrate coated $CoFe_2O_4$ NPs.

Vibrational modes	Frequency (cm^{-1}) Citric acid	Frequency (cm^{-1}) Trisodium citrate	Frequency (cm^{-1}) Citrate-coated NPs
ν_s (C=O, COOH)	1709	—	1676 (chemisorbed)
ν_{as} (COO^-)	—	1572	1572 (free)
ν_s (COO^-)	—	1390	1390
ν (CH_2)	1406(sc)/1078(w)	Convolved withν_s (COO^-) /1078(w)	Convolved withν_s (COO^-) /1078(w)
Combination of ν (COO^-) and $\delta(COO^-)$	—	1300-1250	1300-1250

ν: stretching, δ: bending, sc: scissor, w: wagging, as: asymmetric, s: symmetric

According to the proposed coordination scheme, at least one carboxylate group results exposed to the solvent, and this group should be responsible for making the surface charged and hydrophilic.[40].

In order to determine the cationic distribution in $CoFe_2O_4$ NPs and to understand the effects of the citrate coating and surface charge on the electronic properties of the three investigated MNP samples, XAS, XMCD and XPS measurements were carried out.

Iron and cobalt $L_{3,2}$ edge XAS was used to estimate the oxidation state of Co and Fe in $CoFe_2O_4$ NPs. The XAS spectra of the three samples were recorded both in TEY (surface sensitive) and TFY (bulk sensitive) mode to investigate the level of uniformity of the chemical

composition. The total integrated intensity of each spectrum was normalized with respect to the L_3 edge to show the relative changes between peak heights.

Fe $L_{3,2}$ and Co $L_{3,2}$ spectra (2p→3d) recorded in TEY for all three $CoFe_2O_4$ NP samples are shown in Figure 4(a,b). TEY spectra clearly indicate that the NP surface has the typical structure of iron oxides, where the octahedral crystal field lifts the degeneracy of both the $2p_{3/2}$ (L_3 edge) and $2p_{1/2}$ (L_2 edge) levels of Fe, generating levels with t_{2g} and e_g symmetry[41–43]. Iron L_3 edge shown in Figure 4(a) consists of a main peak at 708.9 eV with a shoulder at 707.4 eV. The L_2 edge, which is separated from the L_3 edge by an energy corresponding to the spin-orbit splitting of 2p core levels, also consists of two peaks (720.8 and 722.4 eV).

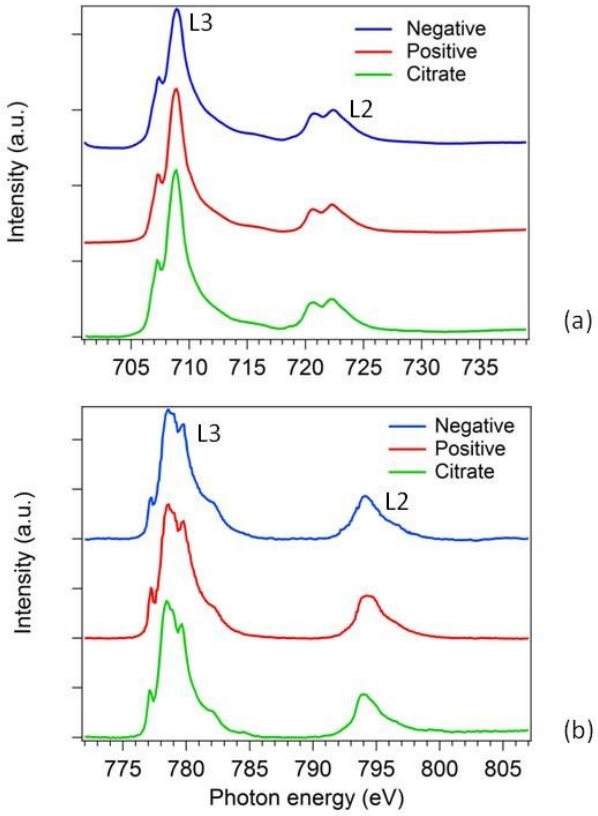

Figure 4. XAS spectra of (a) Fe $L_{3,2}$ edge and (b) Co $L_{3,2}$ edge of negatively and positively charged uncoated, and citrate coated $CoFe_2O_4$ NPs recorded in TEY mode.

The absence of detectable differences between the surface-sensitive TEY spectra of uncoated and citrate coated NPs indicates that the oxidation state of Fe cations on the surface is not affected by the presence of the citrate shell. The bulk sensitivity of TFY XAS (not shown) evidenced that the bulk electronic structure of the $CoFe_2O_4$ NPs is the same as that of the surface.

The corresponding Co $L_{3,2}$ spectra (2p→3d), recorded in TEY, are displayed in Figure 4(b). They exhibit the typical multiplet structure of octahedral Co^{2+} compounds.[42–44]. The L_3 edge is characterized by three peaks at 777.1, 778.5 and 779.7 eV, and by a shoulder at 782 eV, and the L_2 edge is around 794 eV.

Again, no differences were detected between citrate coated and uncoated $CoFe_2O_4$ NPs, showing that the uppermost layer of Co ions is not affected by the citrate shell.

The experimental XAS spectra of Fe $L_{3,2}$ and Co $L_{3,2}$ were compared to those calculated using the LFM model to assign the corresponding cationic contribution to each spectral feature (see experimental section). The simulated spectra were obtained from a weighted superposition of the individual spectra of each cationic species in the sample calculated considering a given crystal field. These determine which cation state is responsible for each peak, and their combination provides the site occupancies of each type of cations.

In the calculations, the Slater integrals *F(dd), F(pd),* and *G(pd)* were reduced to 80% [42,43,45] to account for overestimation of the electron repulsion in solid compounds, and all the spectra were broadened by a Lorentzian with a half-width of 0.2(0.3) eV and by a Gaussian with a half-width of 0.2 eV [42,46,47].

Figure 5(a) shows the Fe $L_{3,2}$ XAS spectrum measured at the citrate-coated $CoFe_2O_4$ NPs together with the simulated one obtained from the linear combination of the LFM calculated spectra of Fe^{2+} octahedral (Oh), Fe^{3+} octahedral (Oh), and Fe^{3+} tetrahedral (Td) cations. The

crystal-field strengths (10Dq) were set to 1.5 for Oh cations, and 0.55 for Td cations, in accordance with previous studies on similar ferrites[42,46,47]. The best combination of individual cationic spectra indicates that most of the Fe^{3+} ions are localized mainly at the Oh sites (72%), while the other Fe^{3+} cations are located at the Td sites (20%). Surprising also some Fe^{2+} species are present at the remaining Oh sites (8%). This was experimentally confirmed by the presence of a small feature at 719.5 eV, that is generally considered a clear signature of octahedrally coordinated Fe^{2+} ions[42]. In fact, Moyer et al. have shown that, in $Co_{(1-x)}Fe_{(2+x)}O_4$ thin film, a small spectral shoulder at the lower energy side of the L_3 peak in Fe XAS spectra increases when the concentration of Co is decreasing. This indicates that, as x increases, Fe is added to the sample in the form of Fe^{2+} octahedral cations, replacing the Co^{2+} ions at the Oh sites.[42,48]

In our case, possible explanations about the unexpected presence of small amount of Fe^{2+} ions in $CoFe_2O_4$ NPs are provided later in the text.

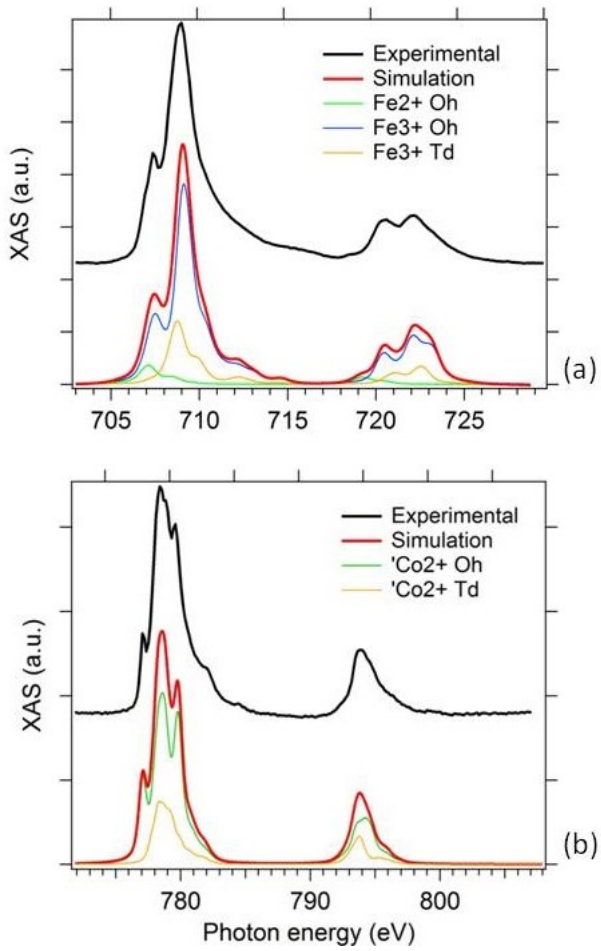

Figure 5. Comparison between the calculated LFM spectra (red curves) and the experimental XAS spectra (black curves) of Fe $L_{3,2}$ edge (a) and Co $L_{3,2}$ edge (b) of $CoFe_2O_4$ NPs. The calculated spectral components corresponding to Fe^{3+} Oh, Fe^{3+} Td and Fe^{2+} Oh cations, and Co^{2+} Oh and Co^{2+} Td cations, respectively, are displayed as well.

The theoretical results for Co $L_{3,2}$ spectrum are displayed in Figure 5(b), where the individual calculated contributions of Co^{2+} octahedral (Oh) and Co^{2+} tetrahedral (Td) cations, and the experimental spectrum of $CoFe_2O_4$ NPs are shown as well. In this case, the crystal field strength used for Co cations is 1.2 for Oh sites and 0.55 for Td sites, in accordance with previous studies[42]. The Co^{2+} Oh cations give strongest contributions (around 75%) that correspond to the

three main features of L_3 in the experimental spectrum. The remaining 25% of Co^{2+} Td cations contribute to the formation of the small shoulder at 782 eV.

The site occupancies of each type of cations is in accordance with previous studies[44,49,50], suggesting that Co cations are exclusively divalent, while Fe consists of a predominating population of trivalent cations together with a small population of some divalent ions, even if the ratio of Co to Fe was expected 1:2. These results suggest that during the $CoFe_2O_4$ NPs' synthesis the majority of the Co cations substitute as Co^{2+} in the Fe^{2+} Oh sites, preserving the overall neutral charge balance of the unit cell. Nevertheless, part of the Co^{2+} can substitute also into the Fe^{3+} Td sites, but this implies an overall negatively charged unit cell. Alternatively, part of the cobalt could substitute as Co^{3+} cations into the Fe^{3+} Td sites, preserving in this way the charge balance[51]. However, the simulation of CoL_{32} XAS spectra do not match very well with the experimental data when Co^{3+} Oh component is introduced (data not shown).

Anyway, there is no sufficient experimental evidence that confirm the oxidation of Co^{2+} to Co^{3+} during the chemical synthesis of $CoFe_2O_4$ NPs[51]. Hence, the precise distribution of 2+ and 3+ charges of Fe and Co cations of Co doped ferrites is still a matter of debate, which cannot be explained only by the charge balance of the unit cell, but further experiments are required.

However, we could also take into account the possibility that some Co and Fe ions are not fully chemically reacted at the synthesis condition.

In any case, the theoretical calculations are in good agreement with the experimental results and confirm a partially inverted spinel structure, as expected for $CoFe_2O_4$ NPs.

Oxygen K-edge XAS spectra of positively and negatively charged uncoated, and citrate coated MNPs dried films were also recorded both in TEY and TFY mode and provided with further details in Figure S1 in the S.I.. The main features of the spectra can be assigned to O 2p

hybridized with the Fe and Co 3d (530 and 534 eV) and 4sp states (536-544 eV). These components, which are typical of oxides such as $CoFe_2O_4$[52–55], are visible in all the samples, indicating that the main signal arises from the NPs cores, where the contribution of the metal oxide is dominant with respect to the surface components responsible for different charges and coatings. This is also corroborated by the fact that the "bulk-sensitive" (TFY) and "surface-sensitive" (TEY) XAS spectra are very similar, suggesting that the components of the citrate coating shell are not detectable because of the low concentration of the ligand coordinated to NPs.

Since XPS is a surface sensitive technique, the core-level spectra of O1s can be used to obtain information about the different surface composition of the three investigated NP samples. Thus, additional XPS measurements of O1s and, Fe and Co 2p core levels were performed for all samples.

XPS spectra of Fe 2p and Co 2p core levels of the three NP samples (Figure S2 (a) and (b), respectively, in the S.I.) further confirm the oxidation state of the two metallic cations in $CoFe_2O_4$, and the superposition of the spectra clearly demonstrate that both the citrate coating and surface charges do not affect the oxidation states of the two cations.

More precisely, the position and separation of Fe $2p_{3/2}$ (710.4 eV) and $2p_{1/2}$ (724eV) peaks, and the presence of the corresponding shake-up satellites at 718.9 eV and 733 eV, respectively, indicates that the dominant state of Fe ions is + 3 [55–57], however the broad band at 710.4 eV may indicate also the presence of Fe^{2+} [42]. In the case of Cobalt 2p, the peak at 780.6 eV with its satellite at 786.6 eV, and the peak at 796.7 eV with its satellite at 803 eV are indicative of Co in the + 2 state[56–58] . The stoichiometric ratio between Fe and Co, quantified by using the intensity

of Fe 2p and Co 2p peaks and taking into account the cross sections of the two elements at the current photon energy, was estimated to be close to 2:1 as expected for $CoFe_2O_4$.

O1s XPS spectra obtained at a low kinetic energy are very sensitive to the presence of molecular species adsorbed on the surfaces. The O 1s spectra of the three samples of NPs shown in Figure 6 and Figure S3 (see S.I.) revealed different chemical composition of the superficial layers adsorbed on the three types of NPs. The broad shape of the spectra indicates presence of several different species containing oxygen. The spectra were further decomposed into four components of similar peak widths. The main component at 529.9 eV, common for all samples, corresponds to O_2^- anions in the $CoFe_2O_4$ spinel crystal lattice[59]. An assignment of the components at higher binding energies is ambiguous due to the overlap of several different groups containing oxygen, signal from substrate, and molecular species adsorbed on the surface during the exposure to ambient atmosphere. Further peak assignments are proposed mainly by referring to photoemission studies on similar systems.

In the case of positively charged $CoFe_2O_4$ NPs, a second significant component was observed at the BE of 531.4 eV. This component can be assigned to the OH_3^+ ions adsorbed on the NP surface. Additional minor components were found at the BE of 532.1 eV and 533.0 eV. The former can be associated with surface and near-surface defect sites with low oxygen coordination, often formally described as O^- species[60,61]. The latter component corresponds to water physisorbed from ambient atmosphere and to the oxygen from the SiO_2 substrate layer, as can be seen by comparing the O 1s spectrum measured on bare substrate (Figure 6, bottom). Three components of comparable intensity can be fitted in O 1s spectra of the negatively charged NPs. The components at 531.3 eV and 532.1 eV can be assigned to the adsorbed OH^- and O^- species, respectively. The O 1s spectrum of citrate coated NPs showed spectral shape similar to

the spectrum of negatively charged particles, which were used as precursor for the citrate coated NPs. Difference was observed in the position of the component previously assigned to hydroxylate groups. This component was shifted to the BE of 531.1 eV in the case of citrate coated NPs and it can be attributed to the presence of COO^- carboxylate groups[62–64]. Some citrate molecules could be bonded to the NPs surface in monodentate form, which would have oxygen peak correspondent to C=O carbonyl bond at the binding energy close to 532.3 eV[26,62]. The capping citrate contains also –OH groups. The corresponding peak is expected around 532.9 eV[26,62].

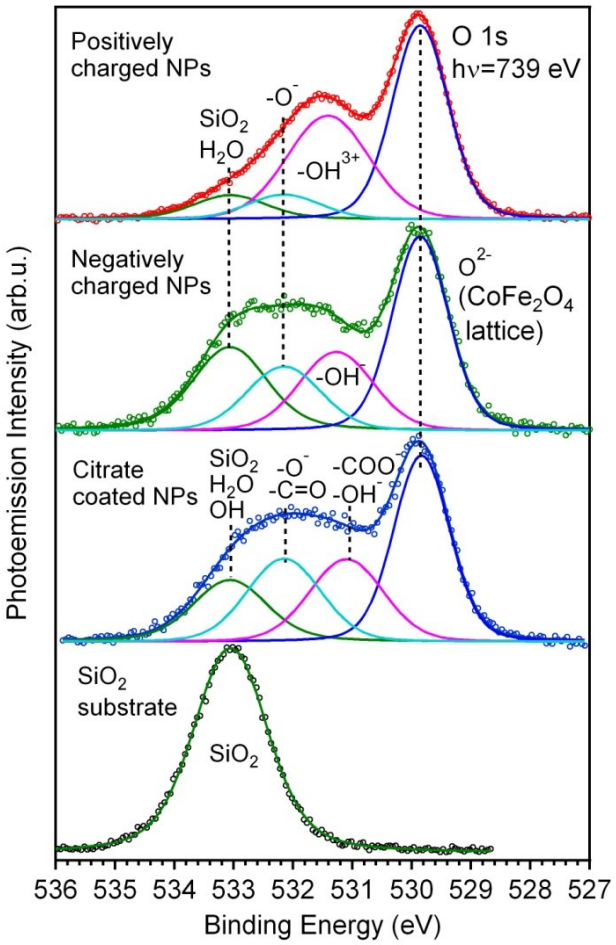

Figure 6. XPS spectra for O1s of positively (red curve), negatively (green curve), citrate coated (blu curve) $CoFe_2O_4$ NPs, and SiO_2 wafer.

Magnetic characterization. The magnetic contributions of each cations (Co and Fe) and further information about the cationic distribution into $CoFe_2O_4$ NPs were obtained by XMCD measurements under an applied magnetic field of 2 T at a temperature of 11 K and in the remnant magnetization condition at 150 K.

In Figure 7 (a,b), Fe $L_{3,2}$ and Co $L_{3,2}$ edge XAS spectra of uncoated $CoFe_2O_4$ NPs are reported with the photo-helicity of incident X-rays parallel (μ+) and anti-parallel (μ-) to the direction of magnetization, and the corresponding XMCD are displayed as well. Fe and Co right-polarized XAS spectra (μ+) were shown with the absorption intensity of L_3 maximum normalized to 1 and the left-polarized (μ-) spectra were scaled accordingly. XMCD spectra were then calculated by subtracting the normalized XAS spectrum measured at opposite helicities. One sees a strong magnetic dichroism for both metals, and the general line shapes are consistent with those reported in the literature[44,49,50].

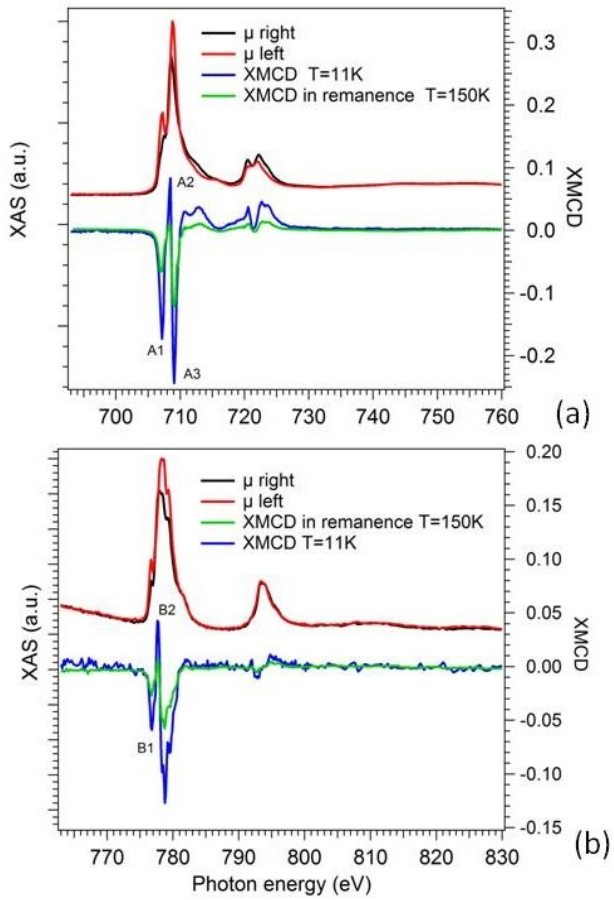

Figure 7. XAS (right and left photon helicity) and the corresponding magnetic difference XMCD spectra of uncoated $CoFe_2O_4$ NPs at the Fe $L_{3,2}$ (a) and Co $L_{3,2}$ edge (b) measured both at 11 K under an applied magnetic field of 2 T and at 150 K at remanence.

The XMCD spectra of Fe $L_{3,2}$ region (Figure 7a) show two negative peaks at 707.2 (A1) and 709eV (A3) corresponding to Fe^{2+} and Fe^{3+} ions at the O_h sites, whereas the positive peak at 708.6 eV (A2) corresponds to the Fe^{3+} cations occupying the T_d sites. The opposite directions of the features A1 and A3 with respect to A2 arise from the antiferromagnetic interaction of the Fe ions at the Oh and Td sites, while the same directions of the peaks A1 and A3 reflects the ferromagnetic interaction between Fe^{2+} and Fe^{3+} in the Oh site.

In the case of Co $L_{3,2}$ edge, the XMCD spectra in Figure 7 (b) show a strong negative peak at 779.3 eV (B1), and a positive one at 778.1 eV (B2). The feature B1 at 779.3eV corresponds to Co^{2+} cations at the O_h sites, while the positive peak B2 at 778.5 eV corresponds to Co^{2+} located at the T_d sites. The opposite directions of features B1 and B2 reflect the antiferromagnetic interaction of Co^{2+} cations at the Oh and Td sites. A comparison between Co and Fe XMCD spectra clearly indicates that Co^{2+} Oh cations are ferromagnetically coupled to Fe^{2+} and Fe^{3+} Oh cations.

The spectra under remnant magnetization conditions clearly indicate that the $CoFe_2O_4$ NPs preserved a fairly large magnetization after the field removal even at higher temperature (150K).

The experimental XMCD spectra of Fe $L_{3,2}$ and Co $L_{3,2}$ were compared to those calculated by LFM model, using the same Slater integrals reduced to 80% adopted for XAS simulation (see above), and a Lorentzian half-width of 0.2(0.3) eV and a Gaussian half-width of 0.15 eV.

The calculations of XMCD data confirm the same cationic site occupancy extrapolated from XAS spectra, suggesting a partially inverted spinel structure of $CoFe_2O_4$ NPs.

Figure 8 shows the Fe $L_{3,2}$ (a) and Co $L_{3,2}$ (b) XMCD spectra together with the simulated ones obtained from the linear combination of the LFM calculated spectra of the single cations distributed among the Oh and Td sites.

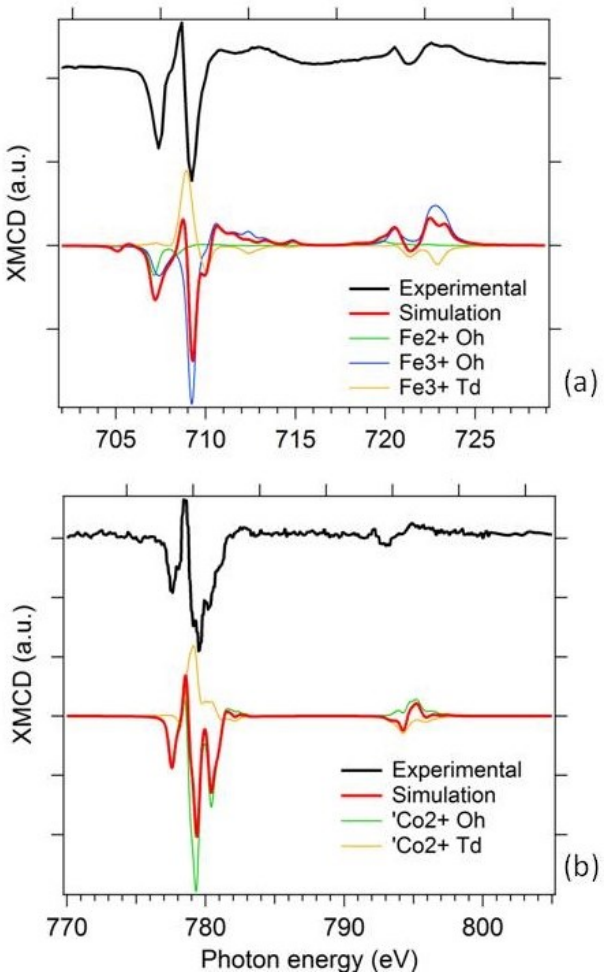

Figure 8. Comparison between the calculated LFM spectra (red curves) and the experimental XMCD spectra (black curves) of Fe $L_{3,2}$ edge (a) and Co $L_{3,2}$ edge (b) of $CoFe_2O_4$ NPs. The calculated spectral components corresponding to Fe^{3+} Oh, Fe^{3+} Td and Fe^{2+} Oh cations, and Co^{2+} Oh and Co^{2+} Td cations, respectively, are displayed as well.

As expected, the combination of individual cationic spectra used for the calculation of Fe L_{32} XMCD spectrum fit pretty well with those used for the simulation of Fe L_{32} XAS spectrum, confirming 72% of Fe^{3+} ions at the Oh sites, 20% of Fe^{3+} cations at the Td sites, and 8% of Fe^{2+} species at the Oh sites. Similarly, for Cobalt L_{32} XMCD spectrum, the combination of 75% of

Co^{2+} Oh cations, and the remaining 25% of Co^{2+} Td cations simulate quite well the experimental result.

Quantative information from XMCD data can be obtained by using the well-defined sum rules that relate the integration of the XAS and XMCD[48] spectra with the orbital (m_L) and spin (m_S) magnetic moments by the following equations[65]:

$$m_L = -4q(10-n_{3d})/3r \quad (1)$$

$$m_S = -(6p-4q)(10-n_{3d})/r \quad (2)$$

where m_L and m_S are given in units of Bohr magnetons per cation (μ_B/cation), and n_{3d} is the 3d electron occupation number per specific cation. The n_{3d} values used for the calculation are 5.6 for Fe, and 7.21 for Co ions, which are expected for $Co_{(1-x)}Fe_{(2+x)}O_4$ magnetic structures[48].

The values of p and q were extracted from the integration of the calculated XMCD spectra (see Figure S4 in S.I.), and the r value by integrating the simulated isotropic XAS spectra of Fe and Co (see Figure S5 in S.I.).

The m_L and m_S of Fe and Co obtained from the sum rules at the temperature of 11 K upon an applied magnetic field of 2 T in the direction parallel to the beam, and at the temperature of 150 K at remanence are reported in Table 3.

Table 3. Orbital (m_L) and spin magnetic (m_S) moments of Fe and Co atoms calculated with XMCD sum rules

T=11 K, H=2T	**m_L** (μ_B/cation)	**m_S** (μ_B/cation)	**m_L/m_S**	**m_L+m_S** (μ_B/cation)
Fe	0.075	1.21	0.062	1.285
Co	0.21	0.32	0.65	0.53
T=150 K, remanence				
Fe	0.044	0.67	0.065	0.714

Co	0.101	0.15	0.67	0.251

The calculated orbital and spin components indicate a m_L close to zero for Fe cations (quenching of the orbital moment) in line with those reported in literature[48,66], while the values of m_S are significantly higher than the m_S reported elsewhere for bulk $CoFe_2O_4$[48]. On the other hand, for Co ions the orbital and spin components are comparable (but slightly lower) to those reported in literature for bulk $CoFe_2O_4$[48].

The lowering of the total magnetic moment of Fe cations in $CoFe_2O_4$ NPs can be associated to nano-structural effects, related to the NP shape and to their reduced size, that result in a larger surface area in comparison to those of bulk materials. The curvature and the large surface area imply that more cations are located at the surface, resulting in a more disordered distribution of the electron spins because of their reduced spin-spin exchange[17,18]. In addition to the nanometric size, also the preparation method of $CoFe_2O_4$ NPs can lead to an increased fractional volume of an oxidized shell at the surface of the NPs, which could contribute to lower the orbital moments of Fe[66].

As expected the orbital and spin components of both Fe and Co atoms are lower at 150 K in remnant magnetization than at 11 K upon an applied magnetic field of 2 T, and their ratio m_L/m_S remain unchanged.

Hysteresis loops measured at 2.5 K on the three $CoFe_2O_4$ NP samples are reported in Figure 9. The coating does not influence appreciably the magnetic properties of the NPs, as can be seen from the values of coercivity (~0.85 T) and relative remnant magnetization (~0.7), as well as from the approach to saturation of the curves. This is not surprising since the high magneto-crystalline anisotropy of cobalt ferrite makes possible changes of surface contribution negligible.

The saturation magnetization values are 64 Am^2/kg (negative), 68 Am^2/kg (positive) and 73 Am^2/kg (citrate). The minor differences in the saturation magnetization values between the three samples can be ascribed to the uncertainty in the determination of the effective concentration of NPs in the dispersion, as opposed to ligands and residual solvent.

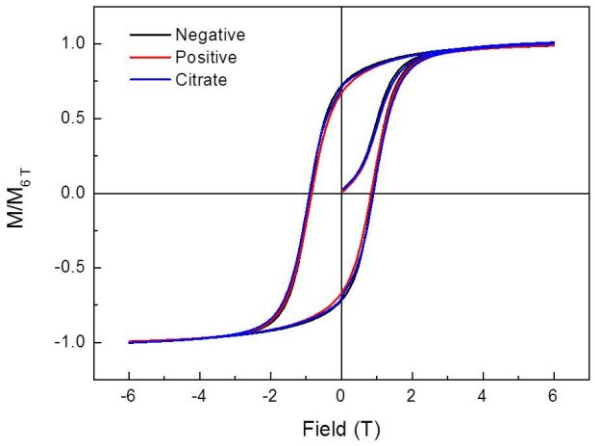

Figure 9. Normalized magnetization curves of negative, positive and citrate-coated $CoFe_2O_4$ NPs measured at 2.5 K.

In Figure 10 are reported the temperature kinetics of the three $CoFe_2O_4$ NPs samples during five minutes of exposition to an AMF (17 kA/m, 183 kHz). The SAR values, evaluated from the initial slopes of the curves, were found comparable for negative and positive $CoFe_2O_4$NPs, being 105 ± 3 and 98 ± 4 W/g of total metals (Fe + Co), respectively. However, a reduction of SAR to 65 ± 7 W/g of total metals (Fe + Co) was observed for the citrate-coated sample. Since the magnetic investigation shows very similar magnetic parameters for all the samples, such discrepancy can be ascribed to a different efficiency in stabilizing NPs by the different surface coatings. The steric effect of citrate molecules combined with the charge repulsion related to the negatively charged carboxylate groups is indeed expected to improve the stabilization of the citrate-coated $CoFe_2O_4$ NPs, by increasing the average separation between particles, thus

reducing the dipolar interactions. The effect of magnetic interactions on hyperthermic efficiency is still under debate[67]. Recently a theoretical study by Burrows et al.[68] reported an increase of the energy losses with interactions for superparamagnetic NPs, due to the enhancement of the energy barrier due to dipole-dipole interactions. In this framework then, it is possible to attribute the higher SAR values observed for negative and positive $CoFe_2O_4$ NPs to the presence of a higher degree of dipolar interactions, due to a less efficient particle stabilization with respect to the citrate-coated sample.

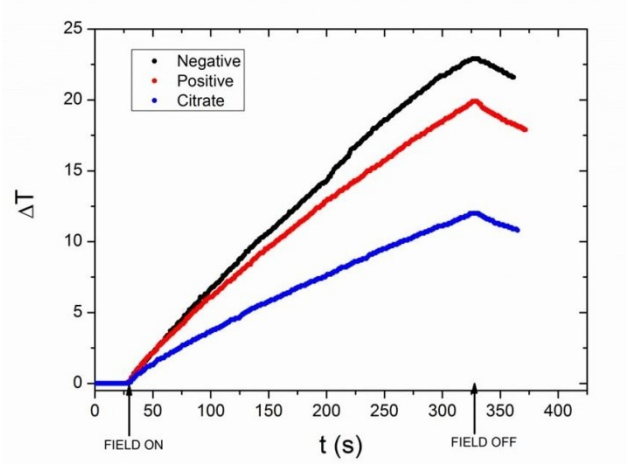

Figure 10. Temperature kinetic curves of $CoFe_2O_4$ NP samples during the exposition to an alternating magnetic field (17 kA/m, 183 kHz, 5 min), starting from a temperature of 25ºC.

4. Conclusions

A simple approach based on co-precipitation method was used for the preparation of $CoFe_2O_4$ colloidal spherical NPs with mean diameter of 12 nm. Different stabilization methodologies were used to obtain well dispersed MNPs in aqueous solution, exploiting both the electrostatic repulsion of uncoated NPs with different surface charge (positive and negative), and a capping agent (citric acid).

The paper reports a detailed spectroscopic characterization of the three investigated MNP samples (positively and negatively charged uncoated MNPs, and citrate coated MNPs) deposited as thin films on Si wafers. In particular, the electronic properties and the oxidation states of the metal ions of $CoFe_2O_4$ NPs were probed by XAS and XPS experiments, confirming that Fe is present dominantly in the +3 state, while Co is in the +2 state for all the samples. The functionalization of $CoFe_2O_4$ NPs by interaction with citric acid was proved by ATR-FTIR and XPS measurements, revealing chemisorption of citrate ions and coordination via one or two of the carboxylate functionalities of the metals on the NP surface.

XMCD and XAS absorption spectra at the $L_{3,2}$ edge of Fe and Co have revealed the presence of a small amount of Fe^{2+} ions located at the O_h sites, while the dominant Fe^{3+} and Co^{2+} cations occupy both the O_h and T_d sites. Finally, hysteresis loops at low temperature were carried out, showing that both uncoated and citrate-coated $CoFe_2O_4$ NPs have a similar magnetic behavior, confirming that the citrate layer does not affect the total anisotropy of the particles. However, the lower SAR value observed for citrate-coated $CoFe_2O_4$ NPs with respect to the negative and positive ones suggests that the hyperthermic properties are influenced by the efficiency of the surface coating in stabilizing the NPs suspension.

In the light of our results, we can conclude that the surface charge and the coating shell of citrate do not alter the electronic properties and the distribution of Fe and Co cations in the oxide cores, and also the magnetic properties remain unchanged. On the other hand, the influence of coating molecules on the hyperthermic efficiency of the nanoparticles deserves further investigation that goes beyond the scope of this paper. It should be stressed, however, that the thorough investigation carried out here restricts any effect to particle dispersibility, as opposed to

alterations of the particle core. This represents an important result for biomedical applications of $CoFe_2O_4$ NPs.

In view of these considerations, our results are the groundwork for future investigations in a liquid environment, aimed at studying how the dispersibility of MNPs in a solvent might perturb the electronic and magnetic properties of coated and uncoated MNPs. The development of special cells consisting of window membranes resistant to UHV conditions and transparent to x-ray photons[69–72] could open the possibility to study MNPs directly in physiological conditions, that is the typical environment required for biomedical applications.

ABBREVIATIONS

NPs nanoparticles; MNPs magnetic nanoparticles; XAS x-ray absorption spectroscopy; XMCD x-ray magnetic circular dichroism; XPS x-ray photoemission spectroscopy; ATR-FTIR attenuated total reflection infrared spectroscopy; VSM vibrating sample magnetometer; AMF Alternating Magnetic Field; UHV ultra-high vacuum; TEY total electron yield; TFY total fluorescence yield; SAXS Small Angle X-ray Scattering; TEM Transmission Electron Microscopy; AC alternating current; MFH magnetic fluid hyperthermia, MRI magnetic resonance imaging; TMAH tetramethylammonium hydroxide

ACKNOWLEDGMENT

The authors thank Federico Salvador and Paolo Bertoch for technical and mechanical support. This work was financially supported by the START-UP project IOM-CNR , MIUR (FIRB project Riname RBAP114AMK) and INSTM-Regione Lombardia (project "MAGNANO").

ASSOCIATED CONTENT

Supporting Information.

Details about ATR FTIR spectra, and XPS spectra in the O1s region of $CoFe_2O_4$ NPs are reported in the Supplementary Information (S.I.). This material is available free of charge via the Internet at http://pubs.acs.org.

AUTHOR INFORMATION

Corresponding Author

Dr. Silvia Nappini*

* e-mail: nappini@iom.cnr.it; fax: +39 040 226 767

Author Contributions

The manuscript was written through contributions of all authors. All authors have given approval to the final version of the manuscript.

Notes

The authors declare no competing financial interest

REFERENCES

1. Reiss, G. & Hütten, A. Magnetic nanoparticles: Applications beyond data storage. *Nat. Mater.* **4,** 725–726 (2005).
2. Hyeon, T. Chemical synthesis of magnetic nanoparticles. *Chem. Commun.* 927–934 (2003). doi:10.1039/B207789B
3. Lu, A.-H. *et al.* Nanoengineering of a Magnetically Separable Hydrogenation Catalyst. *Angew. Chem.* **116,** 4403–4406 (2004).

4. Tsang, S. C., Caps, V., Paraskevas, I., Chadwick, D. & Thompsett, D. Magnetically Separable, Carbon-Supported Nanocatalysts for the Manufacture of Fine Chemicals. *Angew. Chem. Int. Ed.* **43,** 5645–5649 (2004).
5. Li, S., Ding, W., Meitzner, G. D. & Iglesia, E. Spectroscopic and Transient Kinetic Studies of Site Requirements in Iron-Catalyzed Fischer−Tropsch Synthesis. *J. Phys. Chem. B* **106,** 85–91 (2002).
6. Nappini, S. *et al.* Controlled drug release under a low frequency magnetic field: effect of the citrate coating on magnetoliposomes stability. *Soft Matter* **7,** 1025–1037 (2011).
7. Nappini, S., Bombelli, F. B., Bonini, M., Nordèn, B. & Baglioni, P. Magnetoliposomes for controlled drug release in the presence of low-frequency magnetic field. *Soft Matter* **6,** 154–162 (2009).
8. Douziech-Eyrolles, L. *et al.* Nanovectors for anticancer agents based on superparamagnetic iron oxide nanoparticles. *Int. J. Nanomedicine* **2,** 541–550 (2007).
9. Tartaj, P., Morales, M. del P., Veintemillas-Verdaguer, S., González-Carreño, T. & Serna, C. J. The preparation of magnetic nanoparticles for applications in biomedicine. *J. Phys. Appl. Phys.* **36,** R182 (2003).
10. Huang, J. Improving the Magnetic Resonance Imaging Contrast and Detection Methods with Engineered Magnetic Nanoparticles. *Theranostics* **2,** 86–102 (2012).
11. Chen, S., Chiang, C. & Hsieh, S. Simulating physiological conditions to evaluate nanoparticles for magnetic fluid hyperthermia (MFH) therapy applications. *J. Magn. Magn. Mater.* **322,** 247–252 (2010).

12. Ito, A. *et al.* Tissue Engineering Using Magnetite Nanoparticles and Magnetic Force: Heterotypic Layers of Cocultured Hepatocytes and Endothelial Cells. *Tissue Eng.* **10,** 833–840 (2004).
13. Franco, A., Machado, F. L. A. & Zapf, V. S. Magnetic properties of nanoparticles of cobalt ferrite at high magnetic field. *J. Appl. Phys.* **110,** 053913–053913–6 (2011).
14. Carta, D. *et al.* A Structural and Magnetic Investigation of the Inversion Degree in Ferrite Nanocrystals MFe2O4 (M = Mn, Co, Ni). *J. Phys. Chem. C* **113,** 8606–8615 (2009).
15. Li, S., Liu, L., John, V. T., O'Connor, C. J. & Harris, V. G. Cobalt-ferrite nanoparticles: correlations between synthesis procedures, structural characteristics and magnetic properties. *IEEE Trans. Magn.* **37,** 2350–2352 (2001).
16. Schultz-Sikma, E. A. *et al.* Probing the Chemical Stability of Mixed Ferrites: Implications for Magnetic Resonance Contrast Agent Design. *Chem. Mater.* **23,** 2657–2664 (2011).
17. Nordhei, C., Ramstad, A. L. & Nicholson, D. G. Nanophase cobalt, nickel and zinc ferrites: synchrotron XAS study on the crystallite size dependence of metal distribution. *Phys. Chem. Chem. Phys.* **10,** 1053–1066 (2008).
18. Jun, Y.-W., Seo, J.-W. & Cheon, J. Nanoscaling laws of magnetic nanoparticles and their applicabilities in biomedical sciences. *Acc. Chem. Res.* **41,** 179–189 (2008).
19. Sahoo, Y. *et al.* Alkyl Phosphonate/Phosphate Coating on Magnetite Nanoparticles: A Comparison with Fatty Acids. *Langmuir* **17,** 7907–7911 (2001).
20. Wooding, A., Kilner, M. & Lambrick, D. B. Studies of the double surfactant layer stabilization of water-based magnetic fluids. *J. Colloid Interface Sci.* **144,** 236–242 (1991).
21. Zhang, Y., Kohler, N. & Zhang, M. Surface modification of superparamagnetic magnetite nanoparticles and their intracellular uptake. *Biomaterials* **23,** 1553–1561 (2002).

22. Studart, A. R., Amstad, E. & Gauckler, L. J. Colloidal Stabilization of Nanoparticles in Concentrated Suspensions. *Langmuir* **23,** 1081–1090 (2007).

23. Laurent, S. *et al.* Magnetic iron oxide nanoparticles: synthesis, stabilization, vectorization, physicochemical characterizations, and biological applications. *Chem. Rev.* **108,** 2064–2110 (2008).

24. Massart, R. Preparation of aqueous magnetic liquids in alkaline and acidic media. *IEEE Trans. Magn.* **17,** 1247–1248 (1981).

25. Bonini, M., Wiedenmann, A. & Baglioni, P. Small Angle Polarized Neutrons (SANSPOL) Investigation of Surfactant Free Magnetic Fluid of Uncoated and Silica-Coated Cobalt−Ferrite Nanoparticles. *J. Phys. Chem. B* **108,** 14901–14906 (2004).

26. Matthew, J. Surface analysis by Auger and x-ray photoelectron spectroscopy. D. Briggs and J. T. Grant (eds). IMPublications, Chichester, UK and SurfaceSpectra, Manchester, UK, 2003. 900 pp., ISBN 1-901019-04-7, 900 pp. *Surf. Interface Anal.* **36,** 1647–1647 (2004).

27. Stavitski, E. & de Groot, F. M. F. The CTM4XAS program for EELS and XAS spectral shape analysis of transition metal L edges. *Micron* **41,** 687–694 (2010).

28. Singh, M. A., Ghosh, S. S. & Shannon Jnr, R. F. A direct method of beam-height correction in small-angle X-ray scattering. *J. Appl. Crystallogr.* **26,** 787–794 (1993).

29. Hergt, R. & Dutz, S. Magnetic particle hyperthermia—biophysical limitations of a visionary tumour therapy. *J. Magn. Magn. Mater.* **311,** 187–192 (2007).

30. Goertz, V., Dingenouts, N. & Nirschl, H. Comparison of Nanometric Particle Size Distributions as Determined by SAXS, TEM and Analytical Ultracentrifuge. *Part. Part. Syst. Charact.* **26,** 17–24 (2009).

31. Bartlett, P. & Ottewill, R. H. A neutron scattering study of the structure of a bimodal colloidal crystal. *J. Chem. Phys.* **96,** 3306–3318 (1992).
32. Schulz, G. V. J. Phys. Chem. 25 (1935).
33. Hayter, J. B. & Penfold, J. An analytic structure factor for macroion solutions. *Mol. Phys.* **42,** 109–118 (1981).
34. Kohler, N., Sun, C., Wang, J. & Zhang, M. Methotrexate-Modified Superparamagnetic Nanoparticles and Their Intracellular Uptake into Human Cancer Cells. *Langmuir* **21,** 8858–8864 (2005).
35. Mudunkotuwa, I. A. & Grassian, V. H. Citric acid adsorption on TiO2 nanoparticles in aqueous suspensions at acidic and circumneutral pH: surface coverage, surface speciation, and its impact on nanoparticle-nanoparticle interactions. *J. Am. Chem. Soc.* **132,** 14986–14994 (2010).
36. Cheraghipour, E. Citrate capped superparamagnetic iron oxide nanoparticles used for hyperthermia therapy. *J. Biomed. Sci. Eng.* **05,** 715–719 (2012).
37. Sahoo, Y. *et al.* Aqueous Ferrofluid of Magnetite Nanoparticles: Fluorescence Labeling and Magnetophoretic Control. *J. Phys. Chem. B* **109,** 3879–3885 (2005).
38. Răcuciu, M., Creangă, D. E. & Airinei, A. Citric-acid-coated magnetite nanoparticles for biological applications. *Eur. Phys. J. E* **21,** 117–121 (2006).
39. Nigam, S., Barick, K. C. & Bahadur, D. Development of citrate-stabilized Fe3O4 nanoparticles: Conjugation and release of doxorubicin for therapeutic applications. *J. Magn. Magn. Mater.* **323,** 237–243 (2011).

40. Max, J.-J. & Chapados, C. Infrared Spectroscopy of Aqueous Carboxylic Acids: Comparison between Different Acids and Their Salts. *J. Phys. Chem. A* **108,** 3324–3337 (2004).

41. Braun, A. *et al.* Pre-edges in oxygen (1s) x-ray absorption spectra: A spectral indicator for electron hole depletion and transport blocking in iron perovskites. *Appl. Phys. Lett.* **94,** 202102–202102–3 (2009).

42. Moyer, J. A., Vaz, C. A. F., Negusse, E., Arena, D. A. & Henrich, V. E. Controlling the electronic structure of Co1-xFe2+xO4 thin films through iron doping. *Phys. Rev. B* **83,** 035121 (2011).

43. Moyer, J. A., Kumah, D. P., Vaz, C. a. F., Arena, D. A. & Henrich, V. E. Epitaxial strain-induced changes in the cation distribution and resistivity of Fe-doped CoFe2O4. *Appl. Phys. Lett.* **101,** 021907 (2012).

44. Wang, B. Y. *et al.* Effect of geometry on the magnetic properties of CoFe2O4–PbTiO3 multiferroic composites. *RSC Adv.* **3,** 7884–7893 (2013).

45. Schmitz-Antoniak, C. *et al.* Electric in-plane polarization in multiferroic CoFe2O4/BaTiO3 nanocomposite tuned by magnetic fields. *Nat. Commun.* **4,** (2013).

46. Kuiper, P., Searle, B. G., Rudolf, P., Tjeng, L. H. & Chen, C. T. X-ray magnetic dichroism of antiferromagnet Fe2O3: The orientation of magnetic moments observed by Fe 2p x-ray absorption spectroscopy. *Phys. Rev. Lett.* **70,** 1549–1552 (1993).

47. Kuiper, P., Searle, B. G., Duda, L.-C., Wolf, R. M. & van der Zaag, P. J. Fe L2,3 linear and circular magnetic dichroism of Fe3O4. *J. Electron Spectrosc. Relat. Phenom.* **86,** 107–113 (1997).

48. Moyer, J. A. *et al.* Magnetic structure of Fe-doped CoFe2O4 probed by x-ray magnetic spectroscopies. *Phys. Rev. B* **84,** 054447 (2011).

49. Kim, C. H. *et al.* Electronic Structure of Vertically Aligned Mn-Doped CoFe2O4 Nanowires and Their Application as Humidity Sensors and Photodetectors. *J. Phys. Chem. C* **113,** 7085–7090 (2009).

50. Hochepied, J. F., Sainctavit, P. & Pileni, M. P. X-ray absorption spectra and X-ray magnetic circular dichroism studies at Fe and Co L2,3 edges of mixed cobalt–zinc ferrite nanoparticles: cationic repartition, magnetic structure and hysteresis cycles. *J. Magn. Magn. Mater.* **231,** 315–322 (2001).

51. Byrne, J. M. *et al.* Controlled cobalt doping in biogenic magnetite nanoparticles. *J. R. Soc. Interface* **10,** (2013).

52. Sherman, D. M. Electronic structures of iron(III) and manganese(IV) (hydr)oxide minerals: Thermodynamics of photochemical reductive dissolution in aquatic environments. *Geochim. Cosmochim. Acta* **69,** 3249–3255 (2005).

53. Groot, F. M. F. de *et al.* Oxygen 1s and cobalt 2p X-ray absorption of cobalt oxides. *J. Phys. Condens. Matter* **5,** 2277–2288 (1993).

54. Cao, C.-Y. *et al.* Low-Cost Synthesis of Flowerlike α-Fe2O3 Nanostructures for Heavy Metal Ion Removal: Adsorption Property and Mechanism. *Langmuir* **28,** 4573–4579 (2012).

55. Moussy, J.-B. From epitaxial growth of ferrite thin films to spin-polarized tunnelling. *J. Phys. Appl. Phys.* **46,** 143001 (2013).

56. Hassnain Jaffari, G. *et al.* Journal of Physics: Condensed Matter. **24,** (2012).

57. Li, M. *et al.* New J. Chemistry. **37,** 3116–3120

58. Zhongpo Zhou *et al.* Applied Surface Science. **254,** 6972–6975 (2008).

59. Zhou, Z. *et al.* Electronic structure studies of the spinel CoFe2O4 by X-ray photoelectron spectroscopy. *Appl. Surf. Sci.* **254,** 6972–6975 (2008).

60. Jiménez, V. M., Fernández, A., Espinós, J. P. & González-Elipe, A. R. The state of the oxygen at the surface of polycrystalline cobalt oxide. *J. Electron Spectrosc. Relat. Phenom.* **71,** 61–71 (1995).

61. Dupin, J.-C., Gonbeau, D., Vinatier, P. & Levasseur, A. Systematic XPS studies of metal oxides, hydroxides and peroxides. *Phys. Chem. Chem. Phys.* **2,** 1319–1324 (2000).

62. Cossaro, A. *et al.* Tailoring SAM-on-SAM Formation. *J. Phys. Chem. Lett.* **2,** 3124–3129 (2011).

63. Wu, N. *et al.* Interaction of Fatty Acid Monolayers with Cobalt Nanoparticles. *Nano Lett.* **4,** 383–386 (2004).

64. Wulser, K. W. & Langell, M. A. Carboxylic acid adsorption on NiO(100) characterized by X-ray photoelectron and high resolution electron energy loss spectroscopies. *Catal. Lett.* **15,** 39–50 (1992).

65. Chen, C. T. *et al.* Experimental Confirmation of the X-Ray Magnetic Circular Dichroism Sum Rules for Iron and Cobalt. *Phys. Rev. Lett.* **75,** 152–155 (1995).

66. Cai, Y. P. *et al.* Orbital and spin moments of 5 to 11 nm Fe3O4 nanoparticles measured via x-ray magnetic circular dichroism. *J. Appl. Phys.* **115,** 17B537 (2014).

67. Martinez-Boubeta, C. *et al.* Learning from Nature to Improve the Heat Generation of Iron-Oxide Nanoparticles for Magnetic Hyperthermia Applications. *Sci. Rep.* **3,** (2013).

68. Burrows, F. *et al.* Energy losses in interacting fine-particle magnetic composites. *J. Phys. Appl. Phys.* **43,** 474010 (2010).

69. Atak, K. *et al.* Nature of the Chemical Bond of Aqueous Fe2+ Probed by Soft X-ray Spectroscopies and ab Initio Calculations. *J. Phys. Chem. B* **117,** 12613–12618 (2013).

70. Gotz, M. D. *et al.* Probing Coster–Kronig Transitions in Aqueous Fe2+ Solution Using Inverse Partial and Partial Fluorescence Yield at the L-Edge. *J. Phys. Chem. Lett.* **3,** 1619–1623 (2012).

71. Seidel, R. *et al.* Origin of Dark-Channel X-ray Fluorescence from Transition-Metal Ions in Water. *J. Am. Chem. Soc.* **134,** 1600–1605 (2012).

72. Blum, M. *et al.* Solid and liquid spectroscopic analysis (SALSA)–a soft x-ray spectroscopy endstation with a novel flow-through liquid cell. *Rev. Sci. Instrum.* **80,** 123102 (2009).

TOC

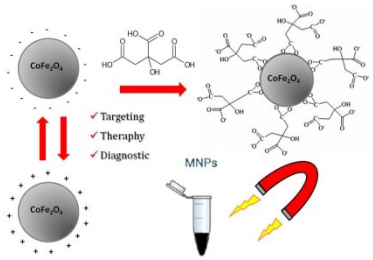

Three types of $CoFe_2O_4$ NPs differently stabilized in aqueous solution were prepared for biomedical applications. A detailed spectroscopic study have shown that the surface modification does not affect the electronic and magnetic properties of the NPs.

.